Computers in Biology and Medicine 171 (2024) 108218

Contents lists available at ScienceDirect

Computers in Biology and Medicine

journal homepage: www.elsevier.com/locate/compbiomed

# Using LDDMM and a kinematic cardiac growth model to quantify growth and remodelling in rat hearts under PAH

Debao Guan [a,c], Lian Tian [b], Wei Li [a], Hao Gao [c,*]

[a] School of Control Science and Engineering, Shandong University, China
[b] Strathclyde Institute of Pharmacy and Biomedical Sciences, University of Strathclyde, UK
[c] School of Mathematics and Statistics, University of Glasgow, UK

ARTICLE INFO

Dataset link: https://github.com/HaoGao/ToFBiVentricle/tree/main/publications/CBM2024

*Keywords:*
Heart failure
Pulmonary arterial hypertension
Growth and remodelling
Kinematic cardiac growth model
LDDMM

ABSTRACT

Pulmonary arterial hypertension (PAH) is a rapidly progressive and fatal disease, with right ventricular failure being the primary cause of death in patients with PAH. This study aims to determine the mechanical stimuli that may initiate heart growth and remodelling (G&R). To achieve this, two bi-ventricular models were constructed: one for a control rat heart and another for a rat heart with PAH. The growth of the diseased heart was estimated by warping it to the control heart using an improved large deformation diffeomorphic metric mapping (LDDMM) framework. Correlation analysis was then performed between mechanical cues (stress and strain) and growth tensors, which revealed that principal strains may serve as a triggering stimulus for myocardial growth and remodelling under PAH. The growth tensors, estimated from in vivo images, could explain 84.3% of the observed geometrical changes in the diseased heart with PAH by using a kinematic cardiac growth model. Our approach has the potential to quantify G&R using sparse in vivo images and to provide insights into the underlying mechanism of triggering right heart failure from a biomechanical perspective.

## 1. Introduction

Cardiovascular disease leads to nearly 74,000 deaths annually in the United Kingdom, with an economic impact of £19 billion per year. Pulmonary arterial hypertension (PAH) is a rapidly progressive and fatal disease, with a median survival of 2.8 years if left untreated [1]. As PAH progresses, the right ventricle (RV) undergoes significant growth and remodelling, including hypertrophy, dilatation, and fibrosis [2]. Eventually, the RV becomes unable to pump adequate amount of blood into the pulmonary arteries, resulting in death. The imbalanced mechanical environment associated with PAH plays a critical role in triggering RV growth and remodelling (G&R). However, there has been limited focus on understanding the G&R of RV during the progression of PAH [3,4], despite the importance of RV being equal to that of the left ventricle (LV) [5,6]. Therefore, there is an urgent need to develop mathematical models that can accurately represent RV biomechanics under both normal and pathological conditions, as well as the mechanisms underlying its evolution.

The phenomenological volumetric growth theory has been extensively utilized in cardiovascular research to model the growth and remodelling of soft tissues [7–9]. However, this theory has limitations in distinguishing between different biological constituents, including myofibres (i.e. myocytes), collagen fibres and ground matrix, which are crucial for understanding the mechanics and mechanobiology of the cardiovascular system. Mechanical stimuli, such as myofiber stretch or stress, are commonly considered as triggers for G&R, leading to two pathological conditions: eccentric and concentric growth [7]. More recently, Guan et al. [10] studied a general hybrid growth of concentric and eccentric patterns in LV triggered simultaneously by stress and stretch by employing an updated Lagrangian constrained mixture approach. While validation of cardiac G&R requires carefully designed experiments, even measuring G&R tensor can be problematic because of tracking biological material points over weeks and months.

Advancements in imaging technologies, such as cardiac magnetic resonance imaging [11,12] and ultrasound imaging [13,14], have facilitated the quantification of regional geometry in vivo. Deep learning approaches have enabled automatic three-dimensional ventricular segmentation of cardiac images, offering faster and more accurate methods for extracting a large volume of 3D geometries [15–17]. This progress has made it feasible to track heart growth in vivo by comparing the geometries of the heart at different pathological states. For example, O'Regan et al. [18] quantified LV remodelling by employing a 3D co-registration approach based on intensity-based similarities and in vivo cine and late gadolinium-enhanced images to monitor ventricular expansion. In an eight-week long volume overload study in pigs,

* Corresponding author.
*E-mail address:* hao.gao@glasgow.ac.uk (H. Gao).

https://doi.org/10.1016/j.compbiomed.2024.108218
Received 12 November 2023; Received in revised form 20 January 2024; Accepted 25 February 2024
Available online 28 February 2024

Costabal et al. [19] measured growth tensor with progression of volume overload, and quantified the correlations between the number of sarcomeres and the expansion of myocytes through machine learning. Meantime, Peirlinck et al. [20] transmit the experimental uncertainties from the organ level down to the cellular scale via their computational growth model, thereby quantifying the concordance between the experimentally observed changes and those predicted by computational approach at the cellular level. They proposed that the elongation in myocytes was predominantly triggered by stretch, and validated a stretch-induced growth tensor elucidated 52.7% of the G&R observed in myocyte morphology. In a recent study, Li et al. [21] proposed a novel method to estimate the apparent growth tensor of the human LV by co-registering four different LV geometries of the same patient, reconstructed from in vivo cine magnetic resonance imaging and late gadolinium-enhanced images at four different time points following myocardial reperfusion.

The Large Deformation Diffeomorphic Metric Mapping framework (LDDMM) is a widely utilized method for non-rigid registration of heart geometries, known for its effective registrations and evolution routines in physical modelling. LDDMM has been applied in various studies investigating the computational anatomy of the heart [22–24] and the brain [24–26]. Diffeomorphisms within the LDDMM framework are regularized by a norm that maps a template geometry to a target geometry, and an optimization procedure is used to determine diffeomorphic routines, which enables statistical analysis of the registration results. For instance, Beg et al. [23] employed LDDMM and geodesic shooting to compute a digital 3D anatomical average atlas of the biventricles from a collection of images, while Biffi et al. [22] utilized the LDDMM framework to estimate the deformation from the mean shape of the LV to different anatomical models of subjects. Guan et al. [5] recently utilized the LDDMM framework to estimate the deformation of a heart from a template shape to a target shape, facilitating the computation of a deformed fibre structure. This approach enables a more reliable estimation of local shape changes.

Shape analysis methods using in vivo non-invasive images for estimating the apparent volumetric growth have been developed successfully in the literature [21]. However, it has not been shown that to which extent the estimated apparent G&R tensor can be informative to the actual myocardial growth. If it is informative, then how it will correlate to imbalanced biomechanical homeostasis. This study aims to develop experiment-informed G&R models to provide new insights into RV failure under PAH. We aim to decipher the onset of adverse growth and remodelling using controlled rat experiments. Firstly, rat heart models with preserved main anatomical structures were reconstructed from ultrasound images, including both the LV and RV. The anatomical changes in the RV and LV at different stages were further qualitatively computed using the LDDMM framework. Finally LDDMM-estimated G&R tensor is validated through a volumetric growth model, and a correlation analysis with biomechanical factors were also carried out. In this work, our contributions include:

- Personalized biventricular models of PAH-affected rats from in vivo ultrasound data;
- Improved LDDMM framework for estimating myocardial growth and remodelling by taking into account soft tissue growth pattern under PAH, such as primary growth along myofibire directions;
- Quantification of growth tensors by mapping a normal heart to a diseased heart;
- Identification of a strong link between growth tensors and myocardial strains, which can account for 83.4% of the geometric change in the diseased heart.

The structure of the paper is organized as follows. Section 2 details the development of image-based PAH models, including both the passive and active myocardial mechanics. Section 3 introduces growth tensor estimation from a control heart to a PAH heart with an improved LDDMM approach. Section 4 firstly presents a correlation analysis between mechanical cues and estimated growth tensors, then followed by a hypothesis test using a stress/strain-driven G&R model. Section 5 further discusses how myocardium adapts under PAH. Finally, concluding remarks can be found in Section 6. All abbreviations in this study are listed in Table 1.

**Table 1**
Abbreviations list.

| Symbol | Meaning | Symbol | Meaning |
|---|---|---|---|
| PAH | Pulmonary arterial hypertension | RV | Right ventricle |
| LV | Left ventricle | G&R | Growth and remodelling |
| LVFW | LV free wall | RVFW | RV free wall |
| EDP | End-diastolic pressure | ESP | End-systolic pressure |
| EDV | End-diastolic volume | ESV | End-systolic volume |
| ES | End systol | ED | End diastole |
| MCT | Monocrotalin | SEP | Septum |
| LDDMM | Large Deformation Diffeomorphic Metric Mapping framework | | |

## 2. Personalized PAH model

### 2.1. Animal model of PAH and acquisition of in vivo data

Details on the animal model of PAH can be found in our previous study [13]. In brief, to develop PAH, male Sprague Dawley rats received a single subcutaneous injection of monocrotaline (MCT; 60 mg/kg). In week 4 post injection, MCT rats developed severe PAH. Control rats received phosphate-buffered saline (PBS; 2 mL/kg). In vivo pressure–volume data were obtained via cardiac catheterization in closed-chest rats using micromanometer, high-fidelity 1.9-F rat pressure–volume catheter (Transonic, London, ON, Canada), as described [13]. Ultrasound images of long- and short-axis view of the hearts were obtained using a high-frequency ultrasound system (Vevo 2100; Visual Sonics, Toronto, ON, Canada), as shown in Fig. 1 for one MCT rat and one control rat with manually delineated wall boundaries.

### 2.2. From image data to rat heart models

To reconstruct 3-D finite element bi-ventricular models, the two ultrasound images (both the long-axis and short-axis images) were first segmented manually as shown in Fig. 1, and then the boundary contours were interpolated in the short-axis view by using in-house developed MATLAB codes for further geometry reconstruction. The detailed steps can be found in Appendix A. A rule-based fibre structure for myocyte aggregation is generated for the reconstructed biventricle with a fibre angle linearly rotated form 60° at the endocardium to −60° at the epicardium [5]. Finally a lumped-parameter model for the pulmonary and systemic circulation systems is attached to the cavities of LV and RV in order to provide physiologically accurate pressure boundary conditions, as shown in Fig. 2(a) and (b). The sets of parameters in the lumped-parameter models are listed in Table A.1 in Appendix A.

### 2.3. Structurally constitutive law

In this study, we consider three main constituents in the myocardium, which are the ground matrix, myofibres and collagen fibres. Collagen fibres are the main unit to bear load when the heart is passively loaded, myofibres provides active tension during cardiac contraction. The total strain energy function for the myocardium is

$$\Psi = \phi_g \Psi_g + \phi_m \Psi_m + \phi_c (\Psi_{cf} + \Psi_{cs} + \Psi_{cn}) \quad (1)$$

where $\Psi_g$, $\Psi_m$, $\Psi_c$ are the strain energy functions associated with the ground matrix, myofibre, collagen fibres, while $\Psi_c$ are further decomposed into three orthogonal responses, parallel to myofibre ($\Psi_{cf}$), cross to myofibre along the sheet direction ($\Psi_{cs}$), and the sheet-normal

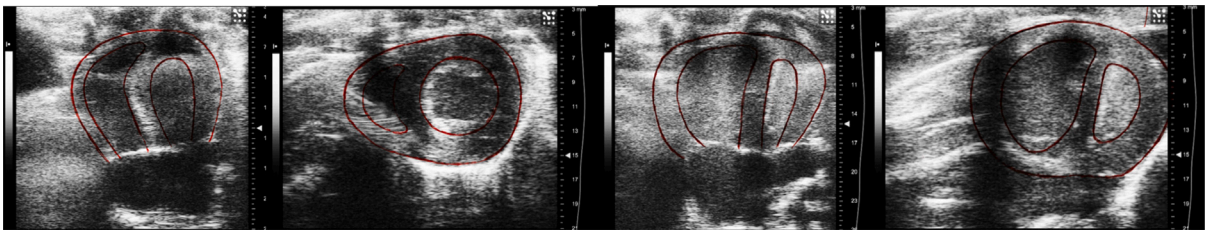

(a) (b)

**Fig. 1.** The long- and short-axis views of the ultrasound images for control (a) and monocrotaline (MCT) rat hearts, respectively. The red curves outline the contours of ventricular walls.

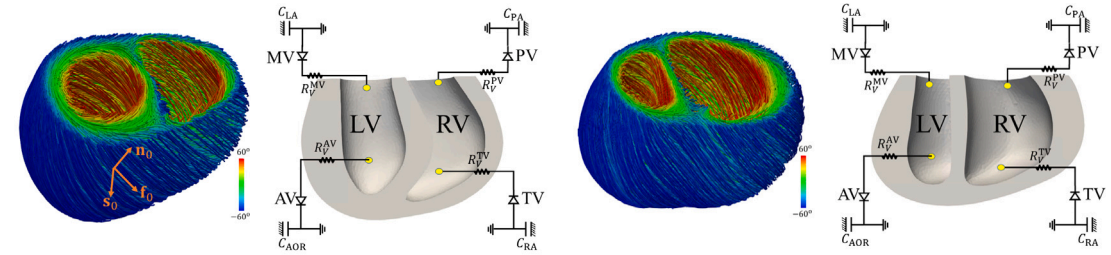


(a) (b)

**Fig. 2.** Reconstructed rat heart models under control (b) and MCT (c) with simple circulation systems and rule-based myofibre structures. $\mathbf{f}_0-\mathbf{s}_0-\mathbf{n}_0$ is the local material coordinate system, in which $\mathbf{f}_0$ is the local mean fibre direction, $\mathbf{s}_0$ is the sheet direction, i.e., transmural direction from endocardium to epicardium, and $\mathbf{n}_0$ is the sheet-normal direction. MV: mitral valve; AV: aortic valve; RA: right atrium; TV: tricuspid valve; PV: pulmonary valve; LA: left atrium; RA: right atrium; AOR: aorta; and PA: pulmonary artery. $R$ is the viscous resistance coefficient of the fluid exchange properties between two connected cavities [27], for example, the resistance between the right ventricle and the right atrium, which effectively represents the pulmonary valve resistance. $C$ is the compliance and is tuned to provide the appropriate pressure–volume response for that cavity.

direction ($\Psi_{\mathrm{cn}}$), respectively. The detailed expressions of the functions are described in Appendix B, and the volumetric fraction for each constituent is $\phi_{\mathrm{g}} = 0.274$, $\phi_{\mathrm{m}} = 0.7$ and $\phi_{\mathrm{c}} = 0.026$. Finally, the total elastic passive stress of the myocardium is

$$\boldsymbol{\sigma}_{\mathrm{p}} = J\mathbf{F}\frac{\partial \Psi(\mathbf{F})}{\partial \mathbf{F}} - p\mathbf{I}, \tag{2}$$

where $J = \det(\mathbf{F})$, $p$ is the Lagrange multiplier to ensure the incompressibility of myocaridum, and $\mathbf{I}$ is the identity tensor. The myocardial active stress is defined by

$$\boldsymbol{\sigma}_{\mathrm{a}} = T_a \hat{\mathbf{m}} \otimes \hat{\mathbf{m}}, \tag{3}$$

where $\mathbf{m}_0$ is the myofibre direction, and $\hat{\mathbf{m}} = \mathbf{m}/|\mathbf{m}|$ with $\mathbf{m} = \mathbf{F}\mathbf{m}_0$, and $T_a$ is determined by a well-established length-tension model [28]. Details of this active contraction model can be found in Appendix B. Finally, the total Cauchy stress is

$$\boldsymbol{\sigma}_{\mathrm{t}} = \phi_{\mathrm{g}}\boldsymbol{\sigma}_{\mathrm{g}} + \phi_{\mathrm{m}}\boldsymbol{\sigma}_{\mathrm{m}} + \phi_{\mathrm{c}}(\boldsymbol{\sigma}_{\mathrm{cf}} + \boldsymbol{\sigma}_{\mathrm{cs}} + \boldsymbol{\sigma}_{\mathrm{cn}}) + \phi_{\mathrm{m}}\boldsymbol{\sigma}_{\mathrm{a}} - p\mathbf{I}. \tag{4}$$

Studies [3,29–31] have shown that the distinct mechanical properties of the LV and the right ventricular free wall (RVFW) lead to different responses to PAH-induced pressure overload. For example, significant RVFW remodelling and adaptation, involving myocardial hypertrophy, increased intrinsic contractility and collagen fibrosis. Therefore, it is necessary to divide the whole heart into two parts, LV and RVFW, in order to capture these complex interactions and their different growth and remodelling mechanism. As shown in Fig. 3(a), we divide the heart into two domains in this study, the LV and the RVFW, and further assuming the LV and RVFW can have different material properties [3]. The detailed approaches to determine material properties of LV and RVFW in the control and MCT hearts are explained in Appendix B. The LV can be further divided in to LV free wall (LVFW) and septum (SEP), as shown in Fig. 3(b)

### 2.4. Cardiac functions of the control and MCT hearts

Fig. 4(a) shows the simulated pressure–volume loops of the control and MCT rat hearts, in which RV end-systolic pressure increases by 100% from 28.9 mmHg in the control heart to 58.2 mmHg in the MCT heart. Reduced RV pump function can be found in the MCT heart, almost halved ejection fraction in the RV (28.5%) compared to the control heart (63.2%). The MCT heart also has a slightly decreased LV ejection fraction compared to the control heart, 56.3% v.s. 66.6%, which may be caused by the dilated RV that pushes the SEP towards the left side as shown in Fig. 1, and thus restrains the diastolic filling in the LV. The deformed shapes at end systole (ES) and end diastole (ED) are shown in Fig. 4(b) contoured by the myofibre stress ($\sigma_{\mathrm{ff}}$). Compared to the control heart, MCT heart has much stiffer myocardium, as evidenced by the material parameters in Table B.1, with much stiffer RV free wall compared to the LV wall. Although the maximum active tension for the MCT heart is twice of that of the control heart, active stress at the ES in RVFW is similar. Interestingly, higher $\sigma_{\mathrm{ff}}$ can be found in the SEP of the MCT heart. In general, the two calibrated cardiac model can reproduce the main characteristics of cardiac functions under control and MCT states, see Table 2 for detailed comparison with measured data.

## 3. Growth tensor estimation

### 3.1. Growth estimation from the two heart models

Here, we estimate the amount of growth from the control heart to the MCT heart by assuming the MCT heart grows from the control heart. *Deformetrica*,[1] an open-source package based on a large deformation diffeomorphic metric mapping (LDDMM), is employed to warp the control heart to the MCT heart as shown in Fig. 2. The loss function ($\mathcal{L}$) is defined by the varifold distance ($D$) between the surfaces of the control ($C_\alpha$) heart and the MCT ($C_\beta$) heart [32], see Appendix C for the detailed definition of $\mathcal{L}$.

After warping $C_\alpha$ into $C_\beta$, the displacement fields for all nodes on the surfaces of $C_\alpha$ can be obtained, denoted as $\mathbf{u}_{\mathrm{Ex}}$. The displacement

[1] http://www.deformetrica.org/.

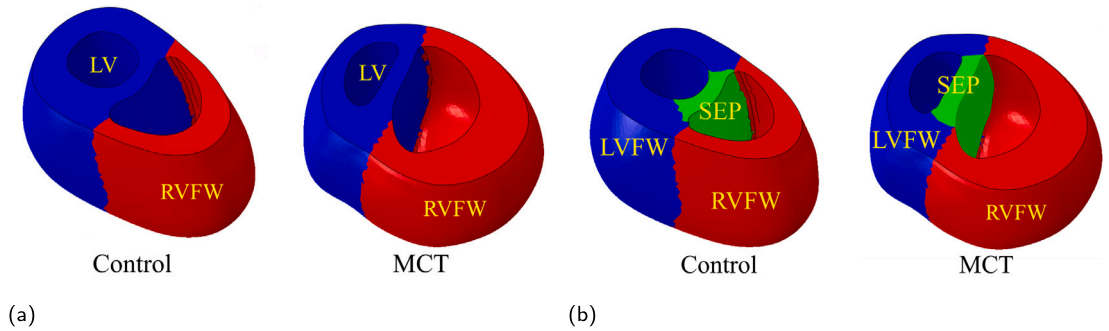


**Fig. 3.** (a) The division of LV and RVFW in the control and MCT hearts, and (b) the LV is further divided into LVFW and SEP.

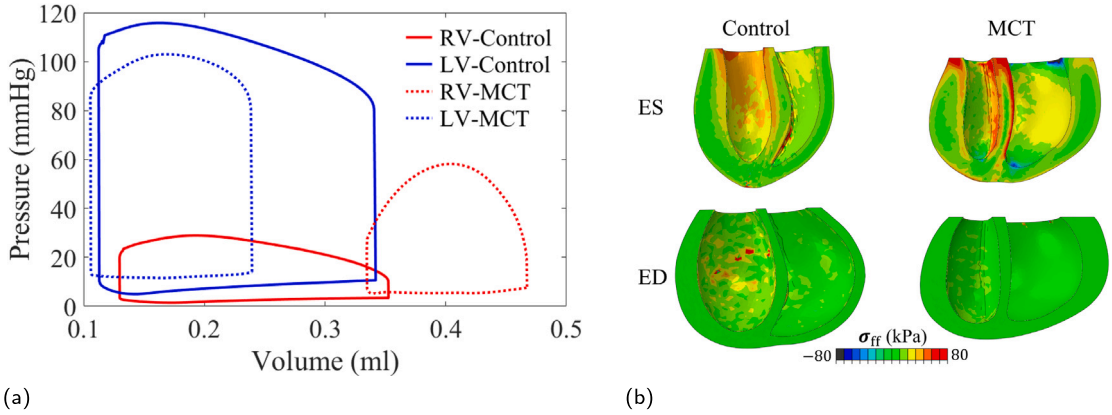


**Fig. 4.** (a) Pressure–volume loops of the Control and MCT rat hearts. (b) Distribution of stress component along fibre direction ($\mathbf{S}_{ff}$) in myocardium at end of systole (ES) and end of diastole (ED).

**Table 2**
Comparison of hemodynamic data between computations (COM) and experiments (EXP).

| Model | | Pressure (mmHg) | | | | Volume (ml) | | | |
|---|---|---|---|---|---|---|---|---|---|
| | | LVEDP | LVESP | RVEDP | RVESP | LVEDV | LVESV | RVEDV | RVESV |
| Control | EXP | 10.7 | 115.3 | 3.5 | 25.8 | 0.346 | 0.120 | 0.355 | 0.134 |
| | COM | 10.7 | 115.8 | 3.5 | 28.9 | 0.341 | 0.114 | 0.353 | 0.130 |
| MCT | EXP | 14 | 98 | 7.7 | 59.5 | 0.225 | 0.085 | 0.466 | 0.334 |
| | COM | 14 | 103 | 7.7 | 58.2 | 0.240 | 0.105 | 0.467 | 0.334 |

vectors of interior nodes within the ventricular wall are then interpolated by solving a Laplace system with Dirichlet boundary conditions, that is

$$\nabla^2\mathbf{u} = 0, \quad \text{with} \quad \mathbf{u} = \mathbf{u}_{\text{Ex}} \text{ at external surface.} \tag{5}$$

Following the finite deformation theory, the mapping tensor of warping the control heart into the MCT heart is defined as

$$\mathbf{G} = \nabla\mathbf{u} + \mathbf{I}. \tag{6}$$

Note that $\mathbf{G}$ and $\mathbf{u}$ are associated with the control model, and det($\mathbf{G}$) represents the volumetric growth amount from the control heart to the MCT heart. The growth amount along each material axis is $G_{ij} = \mathbf{G} : \boldsymbol{i}_0 \otimes \boldsymbol{j}_0$ with $i, j \in \{\text{f, s, n}\}$.

Because Eq. (5) only takes into account the distance between the two surfaces, we further include two cues to improve the quality of warped mesh network with an updated loss function, that is

$$\mathcal{L} = \mathcal{D} + \mathcal{V} + \mathcal{Q}, \tag{7}$$

where $\mathcal{V}$ is the normalized volume variance of elements and $\mathcal{Q}$ measures the quality of each four-node tetrahedral element. Further details of $\mathcal{V}$ and $\mathcal{Q}$ can be found in Appendix C. To further quantify effects of $\mathcal{D}$, $\mathcal{V}$ and $\mathcal{Q}$ when mapping from the control heart to the MCT heart, four cases are introduced, they are

- Case 1: $\mathcal{L} = \mathcal{D}$;
- Case 2: $\mathcal{L} = \mathcal{D} + \mathcal{Q}$;
- Case 3: $\mathcal{L} = \mathcal{D} + \mathcal{V}$;
- Case 4: $\mathcal{L} = \mathcal{D} + \mathcal{Q} + \mathcal{V}$.

### 3.2. Results: Improvement of LDDMM

Fig. 5(a) shows the mapping displacements on external surfaces from Case 1, and Fig. 5(b) shows the mapped interior nodes within the cardiac wall from Case 4 after the interpolation using Eq. (5). Compared to Fig. 5(a), it can be seen that by including more cues in the loss function $\mathcal{L}$, a much more homogenized element volume can be found in Fig. 5(b). Fig. 5(c) illustrates the goodness of fit of each case compared to the MCT heart (solid blue colour). All external surfaces seem to match the targeted MCT heart, while final loss function varied for each case as shown in Fig. 5(d). Although the least varifold distance ($D$) is in Case 1, while the values of $\mathcal{Q}$ and $\mathcal{V}$ in Case 1 are about the twice of those from cases 2–4, indicating the mapped computational mesh quality could be inhomogeneous, such as excessive squeezed or distorted elements. Cases 2 and 3 have similar values in $D$, $\mathcal{V}$ and $\mathcal{Q}$, by including both $\mathcal{Q}$ and $\mathcal{V}$ in the loss functions, it seems the improvement is minor (Case 4). Interested readers refer to Appendix D for further explanations. Fig. 6 further summarizes the volumetric growth ratio

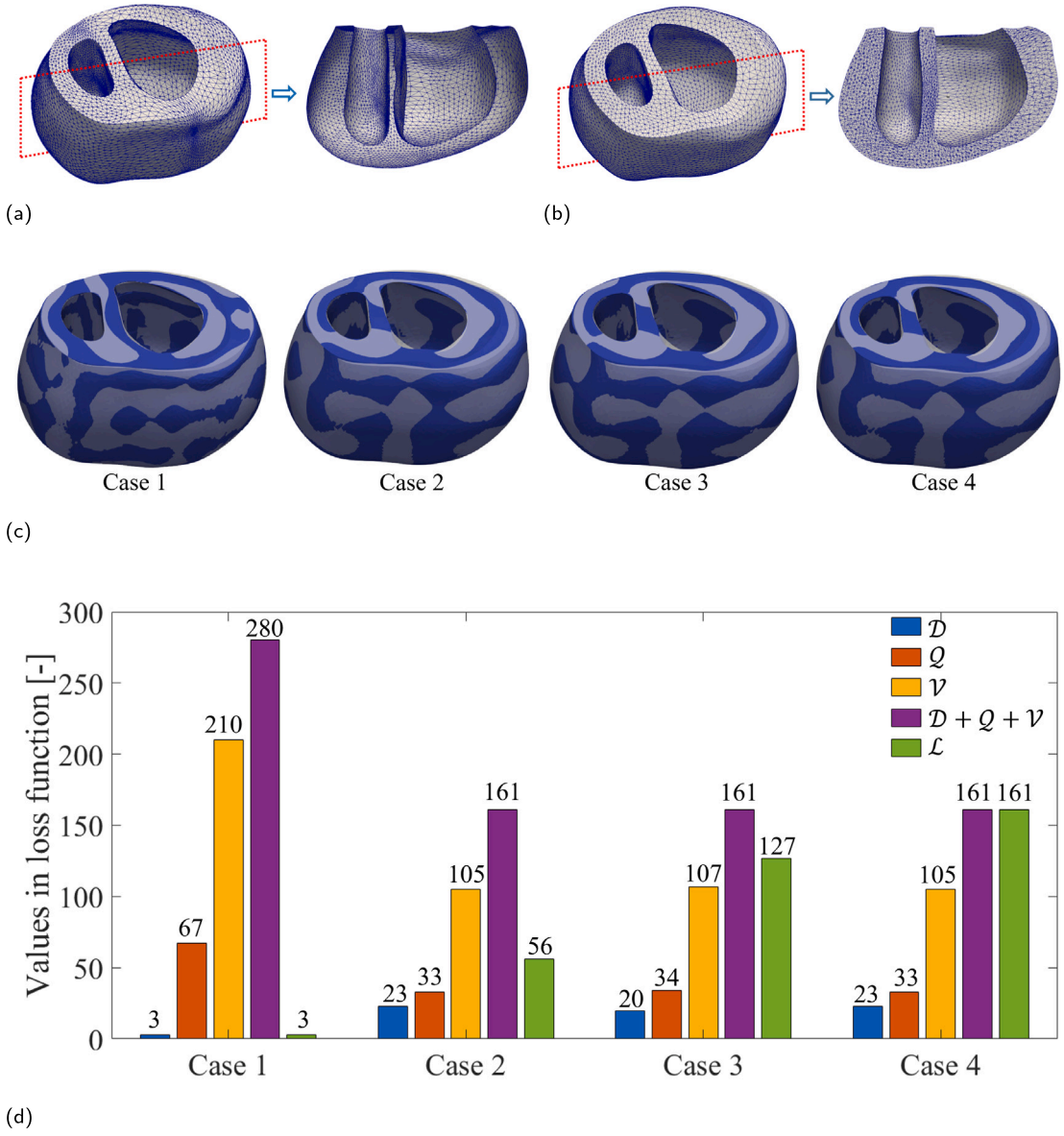


**Fig. 5.** From the control heart to the MCT heart, (a) warped heart by using the original LDDMM algorithm, which is a surface mesh, and (b) warped heart by using the updated LDDMM algorithm, which is a tetrahedral mesh. (c) Fitness between the warped control heart and targeted MCT heart in the four cases, and corresponding values of each term in the loss function (d).

(det **G**) and element quality in LVFW, RVFW and SEP. Again, it can be found that by including extra cues in the loss function, the variations of det **G** and $q$ are reduced for each individual region though the difference among different cues is minor. Given that Case 2 has the least loss function $\mathcal{L}$ and the improvement of including $\mathcal{V}$ is minimal, therefore, only $\mathcal{Q}$ is included in the loss function in the following analysis (see Table 3).

The growth tensors from the control heart to the MCT heart are then estimated using Eq. (6), and further summarized for the representative element sets from LVFW, RVFW and the SEP, respectively. The highest growth occurs in RVFW with an average value of $\bar{J} = 2.34$, followed by LVFW with $\bar{J} = 1.22$, whilst the least volumetric growth in the SEP with $\bar{J} = 1.15$. Fig. 7 compares the mean value of each entry of the growth tensor, in which growth mainly occurs along the fibre, sheet and sheet-normal axial directions. Specifically, the LV has balanced growth along three orthogonal axes, whilst RV grows mainly along the sheet direction, i.e., thickening RVFW. The SEP may have complex growth and remodelling process, for example, the shear growth components are much bigger than those of LVFW and RVFW when elements are compressed along the sheet direction and stretched along the other two fibre directions.

**Table 3**
Summary of mean and standard error in the four cases.

| | Volume change ratio (det(G)) | | | |
|---|---|---|---|---|
| | Case 1 | Case 2 | Case 3 | Case 4 |
| LVFW | 1.2912 ± 0.4799 | 1.2166 ± 0.2780 | 1.2179 ± 0.2826 | 1.2154 ± 0.2764 |
| RVFW | 2.3036 ± 1.3414 | 2.3591 ± 1.0031 | 2.3574 ± 1.0140 | 2.3612 ± 1.0017 |
| SEP | 1.1336 ± 0.6405 | 1.1458 ± 0.5640 | 1.1525 ± 0.5652 | 1.1407 ± 0.5628 |
| | Quality ($q$) | | | |
| | Case 1 | Case 2 | Case 3 | Case 4 |
| LVFW | 0.6391 ± 0.1427 | 0.6797 ± 0.1256 | 0.6786 ± 0.1261 | 0.6799 ± 0.1256 |
| RVFW | 0.5458 ± 0.1710 | 0.6208 ± 0.1338 | 0.6181 ± 0.1351 | 0.6213 ± 0.1334 |
| SEP | 0.4590 ± 0.1533 | 0.5426 ± 0.1786 | 0.5418 ± 0.1773 | 0.5415 ± 0.1790 |

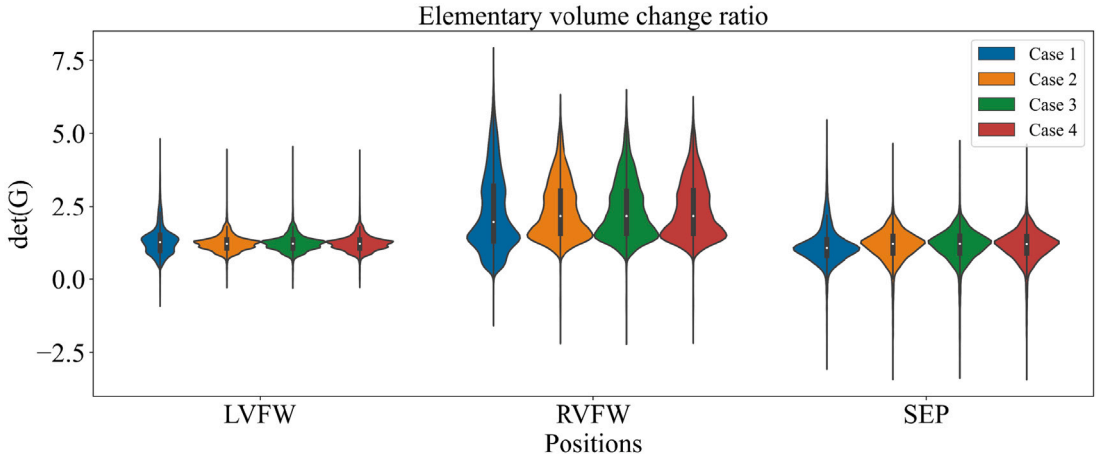


(a)

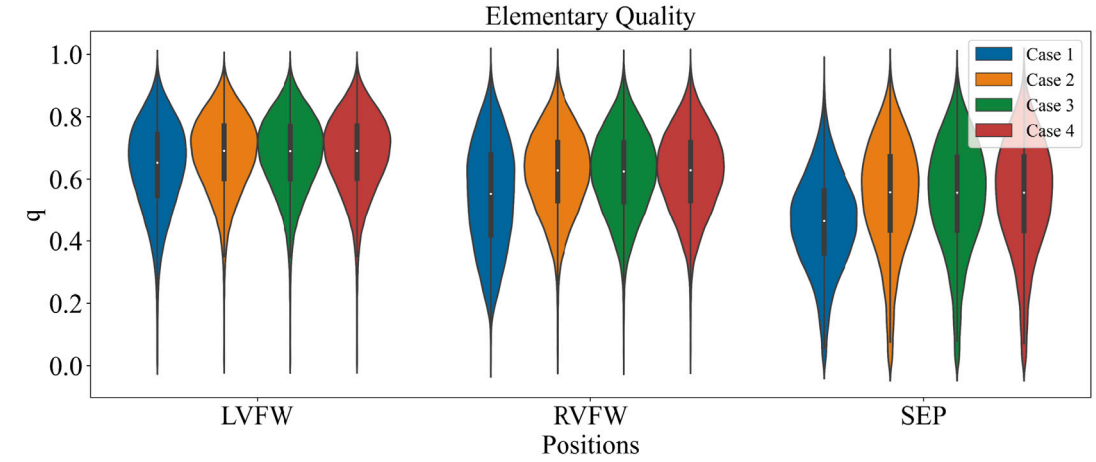


(b)

**Fig. 6.** Violin plot of elementary volume change ratio (a) and elementary quality (b) at LVFW, RVFW and SEP, respectively, from the control to the MCT heart by using the different total loss function in each case.

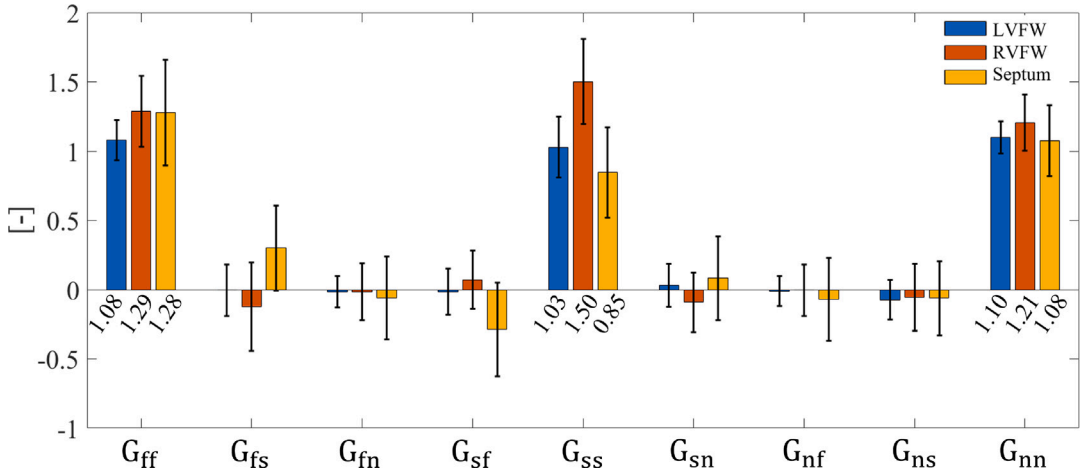


**Fig. 7.** Mean value of each entry in deformation tensors of elements at different regions in case 2.

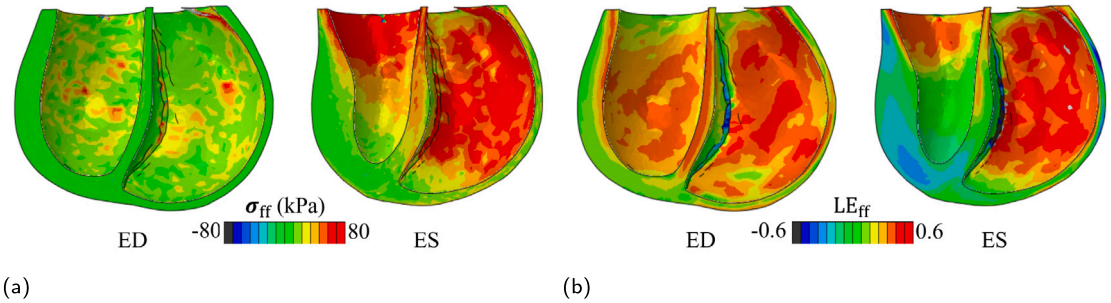


**Fig. 8.** (a) Distributions of myofibre stress component $\sigma_{ff}$ (a) and logarithm strain component $LE_{ff}$ (b) in the deformed synthetic heart model at ED and ES, respectively.

## 4. Stress/strain-driven G&R: hypothesis test

### 4.1. Correlation analysis

Existing studies have suggested that mechanical cues (stress and stretch) can play a significant role in pathological myocardial growth [7,9,10,33]. Here, we further carried out the correlation analysis between the changes in logarithm strain $\Delta LE_{ii}$ and stress $\Delta\sigma_{ii}$ along the material coordinates and estimated growth quantities ($G_{ii}$). To determine the mechanical cues, the boundary conditions of the MCT heart were applied to the control heart, denoted as a synthetic heart model, and the calculated mechanical cues minus the corresponding values in the control state are denoted as $\Delta LE_{ii}$ and $\Delta\sigma_{ii}$. Spearman's rank correlation coefficient is employed here to assess how strong the correlation between two variables is.

Fig. 8 presents the distributions of $\sigma_{ff}$ and $LE_{ff}$ within the deformed synthetic heart model at both ED and ES phases. A comparison with the loaded control heart depicted in Fig. 4(b) reveals notable distinctions. The synthetic heart exhibits larger EDVs in both LV and RV, primarily due to elevated EDPs associated with the MCT model. Notably, the RV experiences a substantial increase in cavity volume, reaching 0.759 ml, approximately double that of the control heart under normal EDP conditions. Although the RV experiences much higher systolic myofibre stresses, the synthetic heart only achieves a mere 14.8% ejection fraction in the RV, a significant reduction compared to the control heart (63.2%). The ejection fractions in the LV has a minor reduction in the synthetic heart, reduced from 66.6% to 62.4%. In the synthetic model, the RVFW experiences greater myofibre strain during passive filling and reduced thickness at ES when compared to the control heart. Thus those biomechanical changes in the myocardium would trigger its G&R [20,34].

The correlation analysis (see Fig. 9) demonstrates that growth tensor correlates with fibre stretch very well, in particular in LVFW. For example, a high correlation coefficient of 0.75 ($p < 0.005$) occurs between $\Delta LE_{ff}$ and $G_{ff}$ in LVFW at the end of diastole, whilst the correlations are not significant at RVFW and the SEP, shown in Fig. 9(a). $\Delta LE_{ss}$ exhibits high correlations with the growth in LVFW at end of systole as shown in Fig. 9(b), such as the correlation coefficient of 0.7 ($p < 0.005$) with $G_{ss}$. Thicken RVFW is mainly positively correlated with the changes of strain along the fibre direction (0.56) and negatively correlated with $\Delta LE_{ss}$ (−0.53). No high correlation is in SEP, and this may be due to the complex growth tensor in the SEP with large shear components.

### 4.2. G&R triggered by mechanical cues

We define the growth tensor in the form of

$$\mathbb{G} = \mathrm{diag}(\mathbf{G}). \tag{8}$$

Following the volumetric growth theory [7], all components share the same total deformation gradient tensor $\mathbf{F}$ from one compatible state to another compatible state, and the total deformation tensor can be decomposed into two parts,

$$\mathbf{F} = \mathbf{F}_e\mathbb{G}, \tag{9}$$

where $\mathbf{F}_e$ is the elastic deformation tensor. To model a stress-free growth in this preliminary test, we reset the parameters in Eq. (B.1) to $a_i = 0$ and $b_i = 1$ with $i \in \{\mathrm{m}, \mathrm{cf}, \mathrm{cs}, \mathrm{cn}\}$ while $a_g = 0.001$ Pa and $b_g = 1$.

To explore the possible growth path from the control heart to the MCT heart, we compared three scenarios for $\mathbb{G}$, which are

1. Every element is assigned with the corresponding $\mathbb{G}_{ff}$, $\mathbb{G}_{ss}$ and $\mathbb{G}_{ss}$ from Eq. (6) directly.
2. The whole heart is firstly divided into two parts, LV and RVFW as shown in Fig. 3, which are further divided into 17 parts according to AHA17 definition [5], respectively. Mean values of $\mathbb{G}_{ff}$, $\mathbb{G}_{ss}$ and $\mathbb{G}_{ss}$ of those elements in each part are applied to all elements in that part.
3. The whole heart is divided into three parts, LVFW, RVFW and SEP as shown in Fig. C.1, and mean values of $\mathbb{G}_{ff}$, $\mathbb{G}_{ss}$ and $\mathbb{G}_{ss}$ of those elements in each part are applied to all elements in that part, i.e. sharing the same $\mathbb{G}$.

The overlapping index between the target heart and the grown hearts is introduced to quantify to which extent the grown heart can be explained by the estimated growth tensor $\mathbb{G}$, that is

$$\mathcal{O} = \frac{2V_o}{V_a + V_b} \times 100\%, \tag{10}$$

where $V_o$ is the intersecting volume between volume $V_a$ and $V_b$. Here, we consider three overlapping indices in terms of the biventricular wall, the LV cavity and the RV cavity, denoted as $\mathcal{O}_{\mathrm{wall}}$, $\mathcal{O}_{\mathrm{LV}}$ and $\mathcal{O}_{\mathrm{RV}}$, respectively.

As shown in Fig. 10(a) where three diagonal entries in the growth tensor ($\mathbb{G}$) of each element are adapted from the corresponding mapping tensor ($\mathbf{G}$) directly, the grown control heart can reproduce 88% of RV cavity volume, while the shape discrepancy mainly occurs at the bulged SEP, overgrown RV at the middle and thinner RV wall at the base. The overlapping indices are also high at the LV ($\mathcal{O}_{\mathrm{LV}} = 83\%$) and biventricular wall ($\mathcal{O}_{\mathrm{wall}} = 82\%$). When all elements in each of 34 regions share the same average growth tensor (Fig. 10(b)), $\mathcal{O}_{\mathrm{LV}}$, $\mathcal{O}_{\mathrm{wall}}$ and $\mathcal{O}_{\mathrm{RV}}$ are lower compared to the first scenario when each local material point is assigned with different $\mathbb{G}$. The poorer overlap is expected since myocardial G&R is spatially heterogeneously. Interestingly, the results from the third scenario (Fig. 10(c)) are similar to the second scenario though the difference can be visually seen in the short-axis view, i.e. excessive circumferential growth in the RV.

## 5. Discussion

Cardiac function is intrinsically tied to its mechanical properties, with stress and strain being critical parameters in understanding the myocardium's response to various conditions [3,10,12,35]. Literature

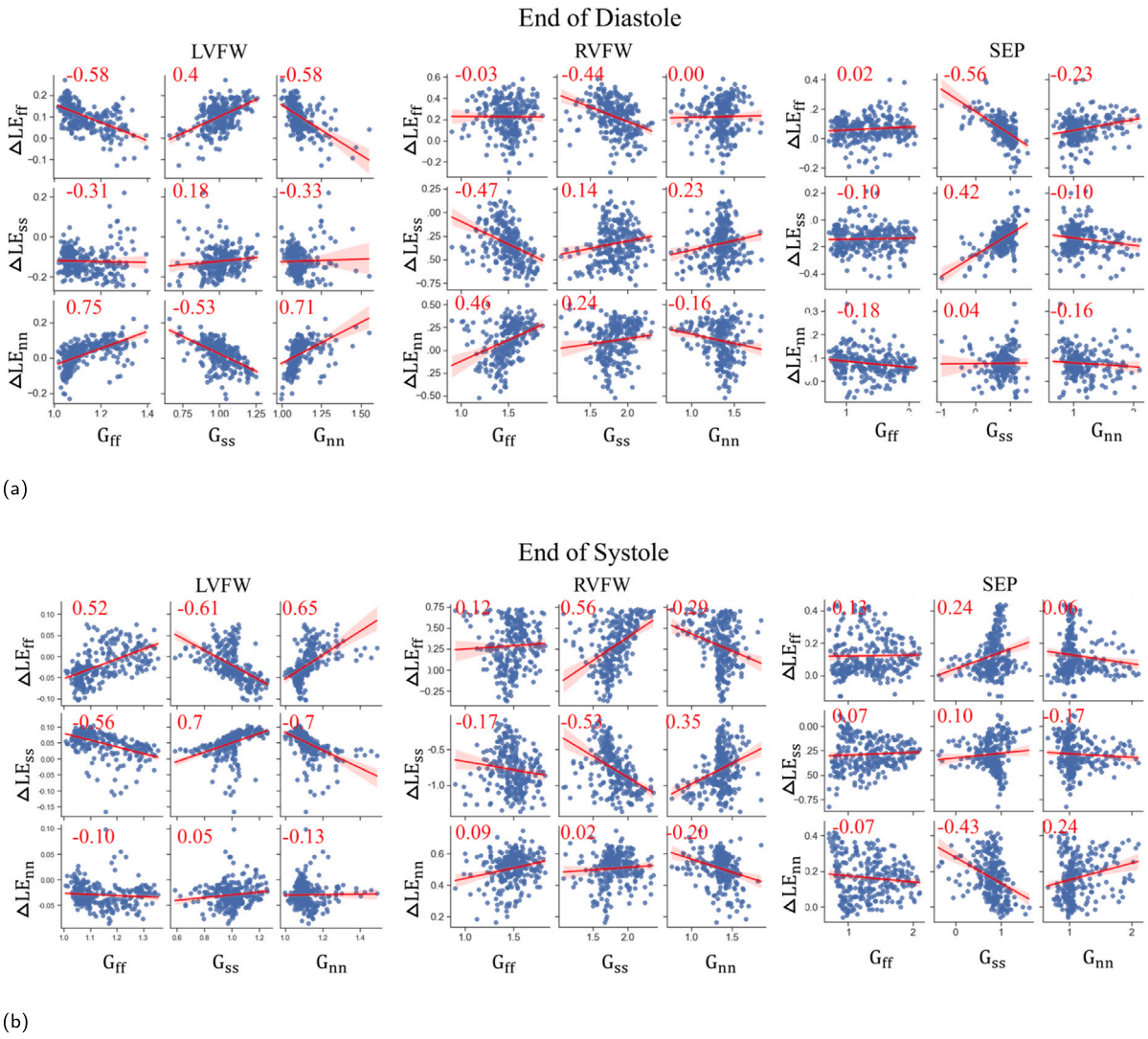


**Fig. 9.** (a) Correlation coefficients and distributions between the varying logarithm strains and growth amounts at the end of diastole (a) and end of systole (b), respectively.

studies, such as those by Avazmohammadi et al. [3,29,36], have documented elevated stress and altered strain patterns in RV, SEP, and LV of PAH patients compared to control heart. Although there is general consistency in the dilated RV cavity with increased stiffness of RVFW while SEP shifts towards LV, achieving precise quantitative agreement between computed and measured data remains challenging. Our computational models not only align with these established patterns of cardiac mechanical alterations but also demonstrate a commendable congruence with the experimentally measured data, reinforcing their validity and utility in the cardiac function studies. Understanding the processes of cardiac G&R is essential for gaining insights into the heart's adaptive and maladaptive responses to both physiological and pathological stimuli, with stress and strain being integral to these processes [7,10]. Our models, calibrated using experimental data including specific EDPs, ESPs, EDVs, and ESVs of LV and RV, have proven their capability in accurately capturing the mechanical responses of the myocardium. This robust alignment indicates that our computed stress and strain values are not only reliable but also possess a high potential in predicting and exploring the triggers for cardiac G&R, particularly in the context of PAH-induced cardiac changes. The matching between our simulation results and measurement data thereby demonstrates our computational models as powerful tools in the cardiac research, offering deep insights into the mechanics of myocardial adaptation and transformation.

The LDDMM method is a well developed method for geometrical mapping in computational anatomy, see examples in heart [24,25] and brain [37]. It produces a nonlinear and smooth metric mapping with a favourable topology-preserving one-to-one properties, and offers a low-dimensional parameterization of diffeomorphisms of the ambient space through control points and momenta. Unique correspondence between the initial geometry and the grown geometry can be established from the acquired diffeomorphism. While one limitation in existing LDDMM, i.e. *Deformetrica*, is purely based on geometrical feature modelling of the geometries, not considering constraints in specific applications, such as regional homogeneous shape change or shape change along specific directions. In this study, we have extended LDDMM-based *Deformetrica* by including elementary quality and volume in the loss function, estimated growth tensors from this improved LDDMM framework seems correlating very well with mechanical cues, which is consistent with stress/strain-induced soft tissue growth and remodelling theory. There are other frameworks which can map different shapes, such as the statistical shape and appearance model [38], or the simplified mapping scheme [21] where a template left ventricular mesh was used for all subjects. Future studies are needed to decide the most appropriate geometrical mapping methods for estimating growth tensors from images.

To the best of our knowledge, this is the first study to quantitatively estimate the growth tensor from a control rat heart to a heart grown under PAH using LDDMM. Patient-specific heart models are reconstructed

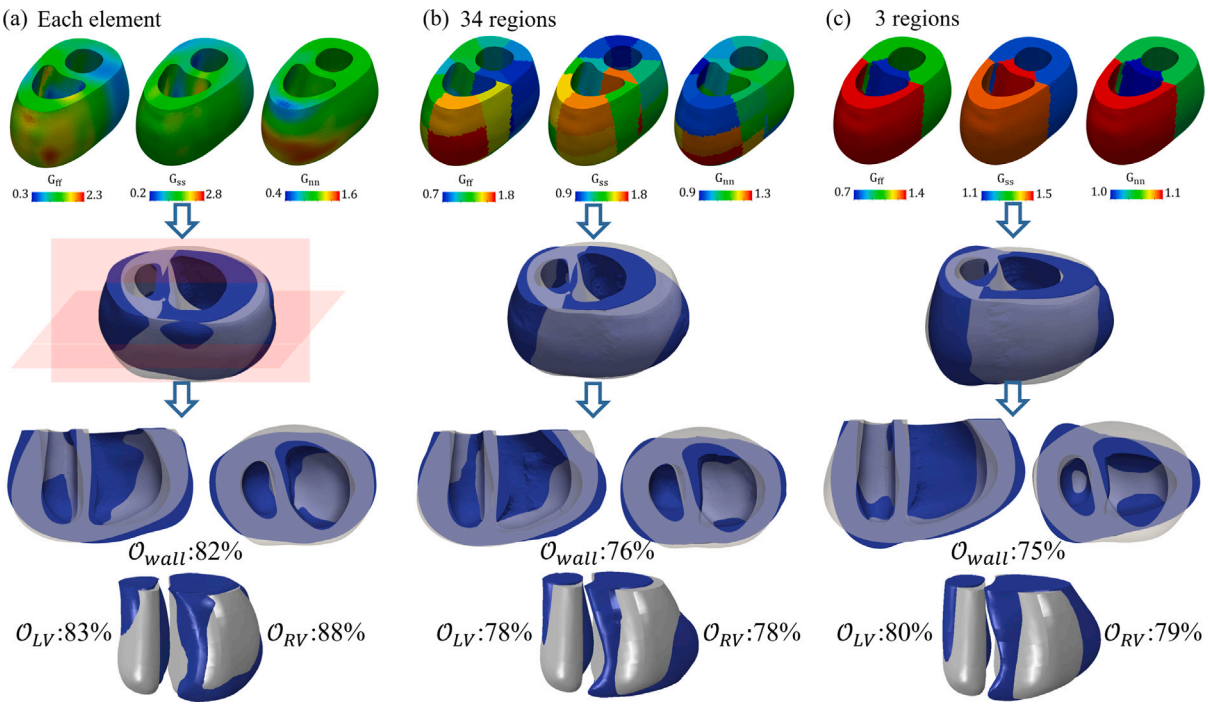


**Fig. 10.** Comparison between the grown control heart (blue) triggered by the estimated growth tensor (grey) under three different scenarios. (a) scenario 1: each element is assigned with different growth tensors; (b) scenario 2, an average growth tensor is assigned in each of 34 regions; and (c) scenario 3, the heart is divided into three regions only and each region has the same average growth tensor.

from ultrasound imaging data and validated by matching measured hemodynamic data. However, the original LDDMM has limitations as it only includes the surface distance between the template and target geometries in the loss function, ignoring the deformation of internal elements. To address this issue, two extra criteria, elementary quality and volume variance, are added to the original loss function, which improve the mapping routine and lead to more homogeneous elementary deformation with higher elementary quality. The preliminary correlation analysis between growth amount and mechanical cues indicates that stretches along three orthogonal directions lead to primary growth. Thus, the growth tensor is proposed by using the diagonal components of LDDMM estimated tensors, which can in fact reproduce more than 82% of the growth of the MCT-induced PAH heart. The growth tensor, induced by stretch and implemented by Peirlinck et al. [20], accounted for a 52.7% mean agreement between the simulations and experiments, lower than the 84.3% mean concordance observed in the current study utilizing a point-wise growth approach, which employs the apparent growth tensor derived from LDDMM. However, Peirlinck et al. [20] elucidated a growth law, characterized by parameters that possess explicit physical interpretations, with values calibrated from experimental data. This growth law offers insightful explanations for the mechanisms driving growth in myocytes and facilitates predictions of growth under specified boundary conditions. The increased average agreement in this study is attributed to the employment of the apparent growth tensor, estimated solely on shape transformation from a control heart to a MCT heart.

In the LDDMM framework, diffeomorphisms are regularized by a norm that plays a significant role in determining the registration quality and the subsequent statistical analysis. Typically, this norm is associated with a kernel, and selecting an appropriate kernel scale involves a trade-off between registration quality and regularity, given that deformations may occur at different scales. In the mesh of the MCT heart, which grows primarily in the RV, elements exhibit homogeneous volumes with high elementary quality that the control heart should replicate using LDDMM. However, applying the original LDDMM leads to excessively stretched or squeezed surface mesh elements, indicating its inability to account for the growth process of the heart. To address this issue, two new criteria, namely elementary quality and volume, are incorporated into the loss function of LDDMM. In order to enhance the registration accuracy of LDDMM, [39] introduced a modification using elastic energy as a new criterion to measure the deformation in LDDMM. Elastic energy was interpreted as a distance in the space of positive definite symmetric matrices, which could handle anisotropic deformations and is inverse-consistent. As manual selection of kernels is difficult, time-consuming, subjective, and prone to errors, Sommer et al. [40] developed a generalization of LDDMM allowing multiple kernels at different scales to be included in the registration process, resulting in significant improvements. Furthermore, the sequential multiscale approach, which involves applying the standard LDDMM shape deformation process at successively smaller physical scales, can also achieve high precision in deforming a source shape into a target shape [41]. The enhancements made in case 2 are similar to those in cases 3 and 4 while only with the addition of the criterion of elementary quality, suggesting elementary quality may play a critical role in the warping routine. Moreover, the approach in case 2 can be employed to deal with different local deformations in one region, where elementary volume cannot be homogenized, which is a limitation of the methods in cases 3 and 4.

We have demonstrated that the model incorporating the element quality metric ($\mathcal{Q}$) alongside the varifold distance ($D$) – as seen in Case 2 – is most effective. This model strikes an balance between accurately matching external surfaces and maintaining high quality in the internal mesh, a critical factor in reliable cardiac modelling. Although Case 1, relying solely on $D$, can effectively match external surfaces, it falls short in internal mesh quality. By adding normalized volume variance ($\mathcal{V}$) to $D$, Case 3 achieves very similar results as in Case 2 but has slightly higher total loss $\mathcal{L}$. The most comprehensive model, Case 4, which incorporates both $\mathcal{Q}$ and $\mathcal{V}$ with $D$, does not significantly outperform Case 2 or Case 3. Therefore, the combination of $D$ and $\mathcal{Q}$ seems a good approach for mapping different cardiac geometries.

From a biomechanical perspective, it pertains to a desirable mechanical condition which is sought by various mechanobiological processes, such as myocyte hypertrophy and fibrosis [7]. While much

remains unclear, it has been established that mechanical stimuli like stress/strain are significant factors in the G&R of soft tissues. In the present study, alterations in myofiber stress and stretch were recorded in the control heart when subjected to the boundary conditions of PAH, and correlations were sought between mechanical stimuli and growth amounts. The results indicate a strong correlation between myofiber stretch and growth during both systole and diastole, whereas no such relationship was observed for myofiber active stress, despite previous studies suggesting its involvement in the computation of concentric growth [7,10,33]. Given that growth is coupled to active tension governed by a function of sarcomere length, the original growth stimuli can also be stretch. On the other hand, elastic strain and stress are coupled through the constitutive relationship and are not mutually independent. So a strain-driven law could also be used as well for wall thickening. For example, Kerckhoffs et al. [42] proposed a single strain-based G&R law to predict concentric and eccentric cardiac G&R, specifically, the fibre strain was used for eccentric G&R, while the cross-fibre strain was used for concentric G&R. The high correlation between mechanical cues and growth mainly occurs along the three orthogonal fibre directions, which are the primary growing direction, and this finding is consistent with the assumption that growth mainly occurs along the fibre direction [7–9,33].

In this study, we have employed Spearman's rank correlation coefficient to assess the relationship between two variables, which is particularly suited for non-parametric data common in biological and medical research [43,44]. This method effectively identifies monotonic relationships, crucial in studies where relationships might not be linear but still consistently increase or decrease. Additionally, it offers robustness against outliers, beneficial in the context of biological variability. In this study, we find that this analysis revealed some correlations between mechanical cues and growth patterns, such as between fibre stretch and growth in the left ventricular free wall. Despite the absence of a strong correlation between myofiber active stress and growth, our findings underscore the complexity of biomechanical changes and myocardial growth and remodelling. Other covariance analysis methods exist, such as maximal information coefficient [45]. Because our ultimate aim is to explore the potential correlations between biomechanical cues and myocardial growth and remodelling, rather than determining the exact correlation between them which is explored in the nonlinear biomechanical growth and remodelling model, therefore, Spearman's method is appropriate in the present study.

At present, it remains uncertain whether average growth or point-wise growth should be employed to simulate the growth process. Point-wise growth appears to be a suitable choice from a phenomenological perspective, as it can effectively reproduce the grown heart under PAH. Conversely, the use of average values for three regions, namely LVFW, RVFW, and SEP, is more efficient since estimating growth amounts from imaging data is more efficient than reconstructing and warping the geometry, although growth amounts at different positions of RVFW may vary. The primary growth is concentrated at RVFW, which exhibits a hybrid pattern of both eccentric and concentric growth, characterized by dilated RV cavity and increased wall thickness. RV growth impels the SEP towards LV, particularly in the long-axis view, resulting in a "D-shaped" profile in the short-axis view. The bulge of the SEP with reduced thickness and increased surface area may serve as an indicator of the severity of RV dilation. In contrast, G&R of LVFW displays eccentric growth characteristics with a thicker wall and a smaller cavity, suggesting that LV and RV may undergo different growth stimulated by distinct growth factors [4]. The disparity in shape between the normal and MCT hearts may be attributed to the limited sample size utilized in our analysis and the fact that the growth tensor estimated in this study is not the true growth tensor, but rather a convenient apparent mapping tensor. Additionally, the data utilized for mathematical modelling of growth from the control heart to the MCT heart inevitably involve remodelling process, despite our efforts to minimize it by setting the strain energy function to a very low value. Ideally, growth tensors should be estimated by tracking the same material point at different times from the same heart. However, since we only had one-time point data after PAH, this study serves as a conceptual study that offers a novel approach for estimating growth tensors from imaging data.

Finally, this study has certain limitations that need to be acknowledged. Firstly, rule-based fibre structure is used in both models, neglecting the remodelling of fibre structure with growth in the MCT heart, as obtaining subject-specific myofibre structure from in vivo imaging data remains a challenging task. Secondly, a simplified open-looped circulation model is adopted, which cannot accurately simulate the realistic blood flow like the one-dimensional model with rich arteries and veins. The parameters in the loss function of LDDMM are not optimized, and their impact on mapping results has not been systematically explored. Thirdly, there is only one-time point data available after PAH, which limits an in-depth exploration of the growing process of the rat heart. Additionally, the modelled growth process is in a unloaded state by minimizing the effect of growth-induced residual stress, which is different from the actual growth that is under constant physiological loading.

## 6. Conclusion

Mathematical modelling of cardiac G&R holds the promise for predicting heart failure and for optimizing treatment strategies to achieve precision medicine in heart disease ultimately. However, the predictive power of those G&R models remains unclear. In this study, we have designed a framework of quantifying G&R in rat hearts under pulmonary arterial hypertension by combining both in vivo imaging data and computational simulations. An improved large deformation diffeomorphic metric mapping framework has been developed to quantify apparent growth tensors by warping a control heart to a diseased heart under pulmonary arterial hypertension, we find that G&R mainly occurs along the myofibre, the sheet and the sheet-normal directions with minimal shear components, and is well correlated to certain myocardial strains. We finally demonstrate that the estimated growth tensor could explain 84.3% of the observed geometrical changes in the diseased heart by using a kinematic cardiac growth model. We have not validated our G&R model in human, future studies shall explore its applicability in patients with PAH-induced right heart failure. Nevertheless, our approach has the potential to quantify myocardial G&R using sparse in vivo data and to provide insights into the underlying mechanism of triggering heart failure from a biomechanical perspective.

## CRediT authorship contribution statement

**Debao Guan:** Formal analysis, Methodology, Writing – original draft. **Lian Tian:** Formal analysis. **Wei Li:** Formal analysis. **Hao Gao:** Conceptualization, Writing – review & editing, Formal analysis.

## Declaration of competing interest

None Declared

## Data availability

The datasets supporting this article have been uploaded to GitHub as part of the electronic supplementary material, https://github.com/HaoGao/ToFBiVentricle/tree/main/publications/CBM2024.

## Acknowledgements

We are grateful for the funding provided by the British Heart Foundation, UK (PG/22/10930). D. Guan also acknowledges the funding

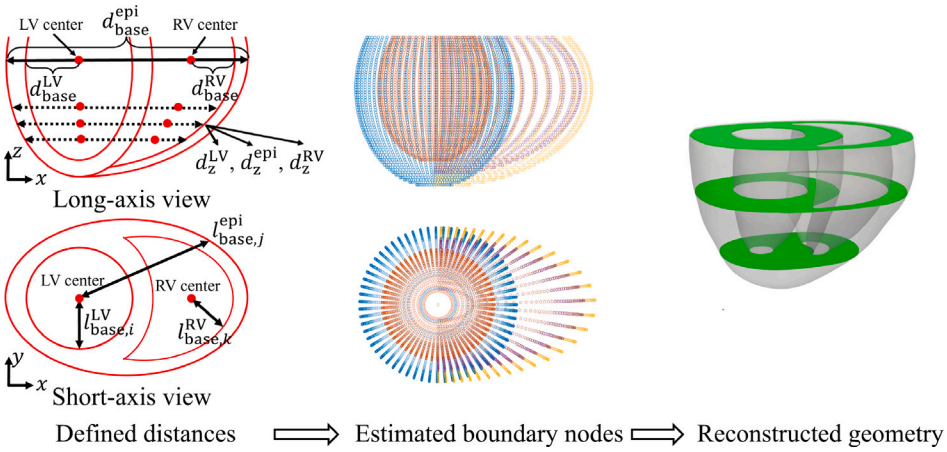


**Fig. A.1.** A schematic illustration on generating a 3D biventricular model from short-axis and long-axis view slices.

**Table A.1**
Parameter values for the lumped circulatory model, and material parameters for passive and active responses. $R$ is the viscous resistance coefficient of the fluid exchange properties between two connected cavities [27], for example, the resistance between the right ventricle and the right atrium, which effectively represents the pulmonary valve resistance. $C$ is the compliance and is tuned to provide the appropriate pressure–volume response for that cavity.

| Lumped circulatory model parameters [5] | | | | | | | | |
|---|---|---|---|---|---|---|---|---|
| Model | $R_V$ (MPa mm$^2$ s/tonne) | | | | $C$ (N/mm) | | | |
| | $R_V^{AV}$ | $R_V^{TV}$ | $R_V^{PV}$ | $R_V^{MV}$ | $C_{AOR}$ | $C_{RA}$ | $C_{PA}$ | $C_{LA}$ |
| Control | 350 | 200 | 280 | 400 | 0.22 | 0.005 | 0.15 | 0.005 |
| MCT | 400 | 600 | 2000 | 700 | 0.16 | 0.005 | 3.0 | 0.005 |

from the school of mathematics and statistics, University of Glasgow, UK through the EPSRC, UK additional funding for mathematical science. W. Li acknowledges the funding from the National Key R and D Program of China (2019YFE0117800), National Natural Science Foundation of China (22176115), Shandong Provincial Key Research and Development Program, China (Major Scientific and Technological Innovation Project) (2021CXGC010506), Shandong Provincial Natural Science Foundation, China (ZR2021MH208).

## Appendix A. Reconstruction of a 3D biventricular model

As shown in Fig. A.1. The interpolated boundary nodes in short-axis views were estimated according to the longitudinal distance to the basal plane. Specifically, In the long-axis view of the base plane, the distance of the LV centre to the LV endocardium is denoted as $d^{LV}_{base}$, while the distance between the two sides of epicardial surface is $d^{epi}_{base}$, and the distance between the RV centre and the RV endocardium is denoted as $d^{RV}_{base}$. Then, for different $z$-axis position, $d^{LV}_z$, $d^{epi}_z$, and $d^{RV}_z$ could be measured in the long-axis view (see Fig. A.1, the top left panel), which were then used to scale the segmented short-axial boundaries at the basal plane. For example, for a short-axial view with $z$ as the longitudinal position, then its boundaries could be defined as follows,

$$l^{LV}_{z,i} = l^{LV}_{base,i}\frac{d^{LV}_z}{d^{LV}_{base}}, \quad \text{and} \quad l^{RV}_{z,k} = l^{RV}_{base,k}\frac{d^{RV}_z}{d^{RV}_{base}}, \quad \text{and} \quad l^{epi}_{z,j} = l^{epi}_{base,j}\frac{d^{epi}_z}{d^{epi}_{base}}. \tag{A.1}$$

in which $i$ represents a boundary node, $l^{LV}_{z,i}$ is the distance of the boundary node $i$ on the LV endocardium to the LV centre at $z$-axis position, similarly for $l^{epi}_{z,j}$, and $l^{RV}_{z,k}$. See the middle panel of Fig. A.1 for the interpolated boundary nodes. Finally, the interpolated nodes were exported into Workbench (ANSYS, Inc. PA USA) for geometry reconstruction as shown in the right panel of Fig. A.1.

In order to provide physiologically accurate pressure boundary conditions, the parameter in the lumped-parameter model for the pulmonary and systemic circulation systems, as shown in Fig. 2, are adjusted based on previous studies [5,46], and their values are listed in Table A.1.

## Appendix B. Structurally constitutive law

Strain energy functions for each constituents are

$$\begin{aligned}
\text{Ground matrix:} \quad & \Psi_g = \frac{a_g}{2b_g}\{\exp[b_g(I_1-3)]-1\} \\
\text{Myofibres:} \quad & \Psi_m = \frac{a_m}{2b_m}\{\exp[b_m(I_{4m}-1)^2]-1\} \\
\text{Collagen:} \quad & \Psi_c = \Psi_{cf}+\Psi_{cs}+\Psi_{cn} \quad \text{with} \\
& \Psi_{cf} = \frac{a_{cf}}{2b_{cf}}\{\exp[b_{cf}(\max(I_{4f},1)-1)^2]-1\} \\
& \Psi_{cs} = \frac{a_{cs}}{2b_{cs}}\{\exp[b_{cs}(\max(I_{4s},1)-1)^2]-1\} \\
& \Psi_{cn} = \frac{a_{cn}}{2b_{cn}}\{\exp[b_{cn}(\max(I_{4n},1)-1)^2]-1\}
\end{aligned} \tag{B.1}$$

where $\Psi_g$, $\Psi_m$, $\Psi_c$ are the strain energy functions associated with the ground matrix, myofibre, collagen fibres, while $\Psi_c$ are further decomposed into three orthogonal responses, parallel to myofibre ($\Psi_{cf}$), cross to myofibre along the sheet direction ($\Psi_{cs}$), and the sheet-normal direction ($\Psi_{cn}$), respectively. Constants $a_i$, $b_i$ with $i \in \{g, m, cf, cs, cn\}$ are material parameters. Here we further assume the collagen fibres along cross-myofibre directions share the same mechanical responses, i.e. $a_{cs} = a_{cn}$ and $b_{cs} = b_{cn}$. Unit vectors $\mathbf{f}_0$, $\mathbf{s}_0$ and $\mathbf{n}_0$ denote the fibre direction, the sheet direction and the sheet-normal in the reference configuration. Myofibre direction ($\mathbf{m}_0$) and collagen fibre direction ($\mathbf{c}_0$) are the same as $\mathbf{f}_0$, and the cross directions are long the sheet direction ($\mathbf{s}_0$) and the sheet-normal ($\mathbf{n}_0$). Given an elastic deformation gradient tensor $\mathbf{F}$, we define

$$\begin{aligned}
&\mathbf{C} = \mathbf{F}^T\mathbf{F}, \quad I_1 = \mathrm{tr}(\mathbf{C}), \quad I_{4m} = \mathbf{m}_0\cdot(\mathbf{C}\mathbf{m}_0) = I_{4f} = \mathbf{f}_0\cdot(\mathbf{C}\mathbf{f}_0) \\
&I_{4s} = \mathbf{s}_0\cdot(\mathbf{C}\mathbf{s}_0), \quad I_{4n} = \mathbf{n}_0\cdot(\mathbf{C}\mathbf{n}_0).
\end{aligned} \tag{B.2}$$

The myocardial active stress is defined by

$$\boldsymbol{\sigma}_a = T_a\hat{\mathbf{m}}\otimes\hat{\mathbf{m}}, \tag{B.3}$$

where $\mathbf{m}_0$ is the myofibre direction, and $\hat{\mathbf{m}} = \mathbf{m}/|\mathbf{m}|$ with $\mathbf{m} = \mathbf{F}\mathbf{m}_0$, and $T_a$ is determined by a well-established length-tension model [28],

$$T_a(t,l) = \frac{T_{max}}{2}\left(1-\exp\left(B\,l_0 - B\sqrt{I_{4m}}\,l_r\right)\right)\left(1-\cos\left(\omega(t,\sqrt{I_{4m}}\,l_r)\right)\right), \tag{B.4}$$

**Table B.1**
Parameter values for the lumped circulatory model, and material parameters for passive and active responses.

| Material parameters | | | | | | | | | | |
|---|---|---|---|---|---|---|---|---|---|---|
| Model | | $a_g$ (kPa) | $b_g$ | $a_m$ (kPa) | $b_m$ | $a_{cf}$ (kPa) | $b_{cf}$ | $a_{cs}$ (kPa) | $a_{cs}$ | $T_{max}$ (kPa) |
| Control | LV | 0.0248 | 0.0017 | 0.0507 | 0.7856 | 0.1254 | 0.7856 | 0.1171 | 0.7703 | 66 |
| | RVFW | 0.0124 | 0.0003 | 0.0319 | 0.4710 | 0.0555 | 0.4717 | 0.0581 | 0.4622 | 38 |
| MCT | LV | 0.2357 | 0.0006 | 0.7773 | 8.5188 | 1.6044 | 8.5201 | 1.5970 | 8.3494 | 150 |
| | RVFW | 2.0742 | 0.0007 | 7.1764 | 12.7793 | 13.9156 | 12.7769 | 14.1486 | 12.5203 | 70 |

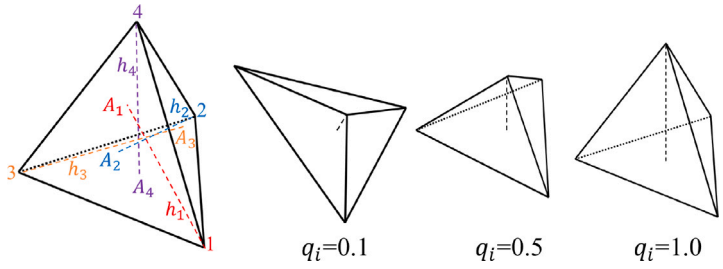


**Fig. C.1.** A sketch of tetra element to compute minimal normalized height.

in which $T_{max}$ is the maximum isometric active tension, $l_0$ is the minimum sarcomere length to produce active stress, $l_r$ is the stress-free sarcomere length, $\omega$ is a time function after the onset of contraction, and $B$ is a constant.

To determine those material parameters in (B.1), a multi-step approach is designed. Firstly, values of passive properties of the RVFW and LV regions for the control and MCT models are obtained from the stress–stretch responses reported in [3]. Secondly, the strain energy function (Eq. (1)) is fitted to the reported data from the first step for both the RVFW and LV of the control and MCT models in a similar approach as [47]. Finally, the parameters $a_i$ and $b_i$ are rescaled by two scaling factors, similar to [48], to match the measured end-diastolic volumes (EDVs) of the LV and the RV for the control and MCT hearts. Finally, the maximum active contraction ($T_{max}$) is determined by matching the measured end-systolic volume (ESV). Parameters in the lumped circulation model are also adjusted to match measured hemodynamic data, including the end-diastolic pressure (EDP) and the end-systolic pressure (ESP). This parameter calibration procedure is similar to our previous works on modelling human hearts [5,10,49]. The sets of parameters for both the control and MCT models are listed in Table B.1.

## Appendix C. Enhanced LDDMM framework

The loss function ($\mathcal{L}$) is defined by the varifold distance between the surfaces of the control ($C_\alpha$) heart and the MCT ($C_\beta$) heart [32], that is

$$\mathcal{L} = D(C_\alpha, C_\beta)^2 = \sum_p \sum_q K(\mathbf{c}_p^\alpha, \mathbf{c}_q^\beta) \frac{((\mathbf{n}_p^\alpha)^T \mathbf{n}_q^\beta)^2}{|\mathbf{n}_p^\alpha||\mathbf{n}_q^\beta|}, \tag{C.1}$$

where $\mathbf{c}_p^\alpha$ and $\mathbf{n}_p^\alpha$ are the centre and the normal of a linear triangle in the triangulated surface $C_\alpha$, accordingly, $\mathbf{c}_q^\beta$ and $\mathbf{n}_q^\beta$ are for the surface $C_\beta$, and $K(\mathbf{c}_p, \mathbf{c}_q) = \exp(-|\mathbf{c}_p - \mathbf{c}_q|^2/\sigma^2)$ is a Gaussian kernel with a width of $\sigma$. Eq. (C.1) can be optimized using the steepest gradient decent or the L-BFGS method implemented in Deformetrica to find a optimal diffeomorphism mapping $\Phi$. Details of the LDDMM framework can be found in [50].

We assume similar amount of growth happens in each region while it can be different among the three regions. Denote the sets of elements $\Omega_{LVFW} = \{l_1, l_2, \ldots, l_{N_1}\}$, $\Omega_{RVFW} = \{r_1, r_2, \ldots, r_{N_2}\}$ and $\Omega_{SEP} = \{s_1, s_2, \ldots, s_{N_3}\}$, in which $l_i$, $r_i$ and $s_i$ are element index, and $N_1$, $N_2$ and $N_3$ are the total numbers of elements in each region with $N = N_1 + N_2 + N_3$ the total number of elements in the biventricle heart. Finally, the normalized volume variance of elements is

$$\mathcal{V} = \frac{w_\mathcal{V}}{N} \sum_{i=1}^{N_1} \left( \frac{N_1 J_{l_i}}{\sum_{i=1}^{N_1} J_{l_i}} - 1 \right)^2 + \frac{w_\mathcal{V}}{N} \sum_{i=1}^{N_2} \left( \frac{N_2 J_{r_i}}{\sum_{i=1}^{N_2} J_{r_i}} - 1 \right)^2 + \frac{w_\mathcal{V}}{N} \sum_{i=1}^{N_3} \left( \frac{N_3 J_{s_i}}{\sum_{i=1}^{N_3} J_{s_i}} - 1 \right)^2, \tag{C.2}$$

where $w_\mathcal{V} = 1000$ to ensure $\mathcal{V}$ is comparable to $D$, and $J_i = \det(\mathbf{G}_i)$. The smaller $\mathcal{V}$, the more homogenized growth in each region.

When interpolating the surface displacements into the interior nodes using Eq. (5), the quality of the elements can be very poor. We now introduce the element quality metric to avoid very poor element quality after the LDDMM mapping. The minimal normalized height is employed to measure the quality of a four-node tetrahedral element, the so-called element's aspect ratio [51], shown Fig. C.1. The height of one tetrahedral element ($h_1$, $h_2$, $h_3$, $h_4$) is computed from each of the four nodes to its opposite face and then divided by the square root of the corresponding face's area ($A_1$, $A_2$, $A_3$, $A_4$). The minimal normalized height is

$$q_i = \min\{\frac{h_1}{A_1}, \frac{h_2}{A_2}, \frac{h_3}{A_3}, \frac{h_4}{A_4}\}/1.24. \tag{C.3}$$

A equilateral tetrahedron has a value of 1, while when the tetrahedron degenerates towards one face, then it has a value of 0. Based on our preliminary tests, we found that elements with a value of $q \geq 0.5$ are suitable for finite element computation. Therefore, we only count the elements with $q < 0.5$ when computing $\mathcal{Q}$, that is

$$\mathcal{Q} = \frac{w_\mathcal{Q}}{N} \sum_{i=1}^{N} (1 - \hat{q}_i), \quad \text{with} \quad \hat{q}_i = \begin{cases} q_i & \text{if} \quad q_i < 0.5 \\ 1 & \text{if} \quad q_i \geq 0.5, \end{cases} \tag{C.4}$$

where $w_\mathcal{Q} = 400$ to ensure $\mathcal{Q}$ is comparable to $D$, and the larger $\mathcal{Q}$, the poorer mesh quality.

## Appendix D. Further explanations to the four cases with the enhanced LDDMM framework

Case 1 ($\mathcal{L} = D$) uses only the varifold distance ($D$) in the loss function. The varifold distance effectively captures the surface discrepancies between the template and target geometries, but it does not account for the internal structure of the mesh. As a result, although the external surfaces match well, the internal mesh may suffer from distortions or inconsistent element volumes, leading to less accurate internal mappings.

Case 2 ($\mathcal{L} = \mathcal{D} + \mathcal{Q}$) adds the element quality metric ($\mathcal{Q}$) to the loss function alongside the varifold distance aims to improve the internal mesh quality by considering the quality of the tetrahedral elements in the computational mesh. The inclusion of $\mathcal{Q}$ helps in ensuring that the internal structure is not overly distorted or squeezed. The similarity in values of $\mathcal{D}$, $\mathcal{V}$, and $\mathcal{Q}$ in this case compared to Case 3 suggests that $\mathcal{Q}$ alone can significantly improve the internal mesh quality.

Case 3 ($\mathcal{L} = \mathcal{D} + \mathcal{V}$) adds the normalized volume variance of elements ($\mathcal{V}$), which measures the homogeneity in the volume of the mesh elements. The inclusion of $\mathcal{V}$ aims to ensure that the volumes of the mesh elements are consistent and not excessively varied, which can affect the accuracy of the mapping.

Case 4 ($\mathcal{L} = \mathcal{D} + \mathcal{Q} + \mathcal{V}$) incorporates both the element quality metric ($\mathcal{Q}$) and the normalized volume variance ($\mathcal{V}$) with the varifold distance ($\mathcal{D}$). The intention is to optimize both the external surface matching and the internal mesh quality and homogeneity. However, the comparison found that the improvement over Cases 2 and 3, where only one additional cue was included, is marginal. This may be partially explained by the fact that the element quality metric $\mathcal{Q}$ could also lead to more homogeneous element volume since a low quality element usually links to a dramatic change in element volume.

Interestingly, incorporating both the element quality metric ($\mathcal{Q}$) and normalized volume variance ($\mathcal{V}$) into the loss function for heart mesh mapping (Case 4) did not significantly enhance results compared to the cases with either $\mathcal{Q}$ (Case 2) or $\mathcal{V}$ (Case 3). This limited improvement could be potentially attributed to several reasons. Firstly, there is some redundancy between $\mathcal{V}$ and $\mathcal{Q}$, since a low quality element may link to a dramatic change in element volume, i.e. extensive distortion in one corner. For that reason, the results from Case 2 and Case 3 are comparable. Secondly, combining multiple metrics adds complexity to the optimization process, potentially leading to trade-offs between optimizing for element quality and volume variance, as shown in Fig. 5, the gain is minimal.

## References


[1] Gilbert E D'Alonzo, Robyn J Barst, Stephen M Ayres, Edward H Bergofsky, Bruce H Brundage, Katherine M Detre, Alfred P Fishman, Roberta M Goldring, Berton M Groves, Janet T Kernis, et al., Survival in patients with primary pulmonary hypertension: results from a national prospective registry, Ann. Intern. Med. 115 (5) (1991) 343–349.

[2] John J. Ryan, Stephen L. Archer, The right ventricle in pulmonary arterial hypertension: disorders of metabolism, angiogenesis and adrenergic signaling in right ventricular failure, Circ. Res. 115 (1) (2014) 176–188.

[3] Reza Avazmohammadi, Emilio A Mendiola, David S Li, Peter Vanderslice, Richard AF Dixon, Michael S Sacks, Interactions between structural remodeling and hypertrophy in the right ventricle in response to pulmonary arterial hypertension, J. Biomech. Eng. 141 (9) (2019).

[4] Pietro Amedeo Modesti, Simone Vanni, Iacopo Bertolozzi, Ilaria Cecioni, Camilla Lumachi, Avio Maria Perna, Maria Boddi, Gian Franco Gensini, Different growth factor activation in the right and left ventricles in experimental volume overload, Hypertension 43 (1) (2004) 101–108.

[5] Debao Guan, Jiang Yao, Xiaoyu Luo, Hao Gao, Effect of myofibre architecture on ventricular pump function by using a neonatal porcine heart model: from DT-MRI to rule-based methods, R. Soc. Open Sci. 7 (4) (2020) 191655.

[6] Arnab Palit, Sunil K Bhudia, Theodoros N Arvanitis, Glen A Turley, Mark A Williams, Computational modelling of left-ventricular diastolic mechanics: Effect of fibre orientation and right-ventricle topology, J. Biomech. 48 (4) (2015) 604–612.

[7] Serdar Göktepe, Oscar John Abilez, Kevin Kit Parker, Ellen Kuhl, A multiscale model for eccentric and concentric cardiac growth through sarcomerogenesis, J. Theoret. Biol. 265 (3) (2010) 433–442.

[8] Martin Genet, MK Rausch, Lik Chuan Lee, S Choy, X Zhao, Ghassan S Kassab, Sebastian Kozerke, Julius M Guccione, Ellen Kuhl, Heterogeneous growth-induced prestrain in the heart, J. Biomech. 48 (10) (2015) 2080–2089.

[9] Lik Chuan Lee, Martin Genet, Gabriel Acevedo-Bolton, Karen Ordovas, Julius M Guccione, Ellen Kuhl, A computational model that predicts reverse growth in response to mechanical unloading, Biomech. Model. Mechanobiol. 14 (2) (2015) 217–229.

[10] Debao Guan, Xin Zhuan, Xiaoyu Luo, Hao Gao, An updated Lagrangian constrained mixture model of pathological cardiac growth and remodelling, Acta Biomater. (2023).

[11] Hossein Yousefi-Banaem, Sasan Asiaei, Hamid Sanei, et al., Prediction of myocardial infarction by assessing regional cardiac wall in CMR images through active mesh modeling, Comput. Biol. Med. 80 (2017) 56–64.

[12] Hao Gao, Andrew Allan, Christie McComb, Xiaoyu Luo, Colin Berry, Left ventricular strain and its pattern estimated from cine CMR and validation with DENSE, Phys. Med. Biol. 59 (13) (2014) 3637.

[13] Lian Tian, Ping Yu Xiong, Elahe Alizadeh, Patricia DA Lima, François Potus, Jeffrey Mewburn, Ashley Martin, Kuang-Hueih Chen, Stephen L Archer, Supracoronary aortic banding improves right ventricular function in experimental pulmonary arterial hypertension in rats by increasing systolic right coronary artery perfusion, Acta Physiol. 229 (4) (2020) e13483.

[14] Vidya K Sudarshan, U Rajendra Acharya, EYK Ng, Ru San Tan, Siaw Meng Chou, Dhanjoo N Ghista, Data mining framework for identification of myocardial infarction stages in ultrasound: A hybrid feature extraction paradigm (PART 2), Comput. Biol. Med. 71 (2016) 241–251.

[15] Jinming Duan, Ghalib Bello, Jo Schlemper, Wenjia Bai, Timothy JW Dawes, Carlo Biffi, Antonio de Marvao, Georgia Doumoud, Declan P O'Regan, Daniel Rueckert, Automatic 3D bi-ventricular segmentation of cardiac images by a shape-refined multi-task deep learning approach, IEEE Trans. Med. Imaging 38 (9) (2019) 2151–2164.

[16] Lukasz Romaszko, Agnieszka Borowska, Alan Lazarus, David Dalton, Colin Berry, Xiaoyu Luo, Dirk Husmeier, Hao Gao, Neural network-based left ventricle geometry prediction from CMR images with application in biomechanics, Artif. Intell. Med. 119 (2021) 102140.

[17] Arash Rabbani, Hao Gao, Alan Lazarus, David Dalton, Yuzhang Ge, Kenneth Mangion, Colin Berry, Dirk Husmeier, Image-based estimation of the left ventricular cavity volume using deep learning and Gaussian process with cardio-mechanical applications, Comput. Med. Imaging Graph. 106 (2023) 102203.

[18] Declan P O'Regan, Wenzhe Shi, Ben Ariff, A John Baksi, Giuliana Durighel, Daniel Rueckert, Stuart A Cook, Remodeling after acute myocardial infarction: mapping ventricular dilatation using three dimensional CMR image registration, J. Cardiovasc. Magn. Reson. 14 (2012) 1–9.

[19] F Sahli Costabal, JS Choy, Kevin L Sack, Julius M Guccione, GS Kassab, Ellen Kuhl, Multiscale characterization of heart failure, Acta Biomater. 86 (2019) 66–76.

[20] Mathias Peirlinck, F Sahli Costabal, KL Sack, JS Choy, GS Kassab, JM Guccione, M De Beule, Patrick Segers, E Kuhl, Using machine learning to characterize heart failure across the scales, Biomech. Model. Mechanobiol. 18 (2019) 1987–2001.

[21] Wenguang Li, Hao Gao, Kenneth Mangion, Colin Berry, Xiaoyu Luo, Apparent growth tensor of left ventricular post myocardial infarction–in human first natural history study, Comput. Biol. Med. 129 (2021) 104168.

[22] Benedetta Biffi, Jan L Bruse, Maria A Zuluaga, Hopewell N Ntsinjana, Andrew M Taylor, Silvia Schievano, Investigating cardiac motion patterns using synthetic high-resolution 3D cardiovascular magnetic resonance images and statistical shape analysis, Front. Pediatr. 5 (2017) 34.

[23] Mirza Faisal Beg, Ali Khan, Computing an average anatomical atlas using LDDMM and geodesic shooting, in: 3rd IEEE International Symposium on Biomedical Imaging: Nano to Macro, 2006, IEEE, 2006, pp. 1116–1119.

[24] Boulbaba Ben Amor, Sylvain Arguillère, Ling Shao, ResNet-LDDMM: advancing the LDDMM framework using deep residual networks, IEEE Trans. Pattern Anal. Mach. Intell. 45 (3) (2022) 3707–3720.

[25] Monica Hernandez, Efficient momentum conservation constrained PDE-LDDMM with Gauss–Newton–Krylov optimization, semi-Lagrangian Runge–Kutta solvers, and the band-limited parameterization, J. Comput. Sci. 55 (2021) 101470.

[26] Jidan Zhong, Desiree Yee Ling Phua, Anqi Qiu, Quantitative evaluation of LDDMM, FreeSurfer, and CARET for cortical surface mapping, Neuroimage 52 (1) (2010) 131–141.

[27] Michael Smith, ABAQUS/Standard User's Manual, Version 6.9, Dassault Systèmes Simulia Corp, United States, 2009.

[28] Julius M. Guccione, L.K. Waldman, Andrew D. McCulloch, Mechanics of active contraction in cardiac muscle: Part II—Cylindrical models of the systolic left ventricle, J. Biomech. Eng. 115 (1) (1993) 82–90.

[29] Reza Avazmohammadi, Emilio A Mendiola, João S Soares, David S Li, Zhiqiang Chen, Samer Merchant, Edward W Hsu, Peter Vanderslice, Richard AF Dixon, Michael S Sacks, A computational cardiac model for the adaptation to pulmonary arterial hypertension in the rat, Ann. Biomed. Eng. 47 (2019) 138–153.

[30] Daniela Vélez-Rendón, Xiaoyan Zhang, Jesse Gerringer, Daniela Valdez-Jasso, Compensated right ventricular function of the onset of pulmonary hypertension in a rat model depends on chamber remodeling and contractile augmentation, Pulm. Circ. 8 (4) (2018) 2045894018800439.

[31] Michael R Hill, Marc A Simon, Daniela Valdez-Jasso, Will Zhang, Hunter C Champion, Michael S Sacks, Structural and mechanical adaptations of right ventricle free wall myocardium to pressure overload, Ann. Biomed. Eng. 42 (2014) 2451–2465.

[32] Nicolas Charon, Alain Trouvé, The varifold representation of nonoriented shapes for diffeomorphic registration, SIAM J. Imaging Sci. 6 (4) (2013) 2547–2580.

[33] Xin Zhuan, Xiaoyu Luo, Volumetric growth of soft tissues from the current configuration, Biomech. Model. Mechanobiol. (2021).

[34] Kirk R. Hutchinson, James A. Stewart Jr., Pamela A. Lucchesi, Extracellular matrix remodeling during the progression of volume overload-induced heart failure, J. Mol. Cellular Cardiol. 48 (3) (2010) 564–569.

[35] Yonghui Qiao, Le Mao, Ying Ding, Ting Zhu, Kun Luo, Jianren Fan, Fluid-structure interaction: Insights into biomechanical implications of endograft after thoracic endovascular aortic repair, Comput. Biol. Med. 138 (2021) 104882.
[36] Reza Avazmohammadi, Michael Hill, Marc Simon, Michael Sacks, Transmural remodeling of right ventricular myocardium in response to pulmonary arterial hypertension, APL Bioeng. 1 (1) (2017).
[37] Michael I Miller, Laurent Younes, J Tilak Ratnanather, Timothy Brown, Huong Trinh, Elizabeth Postell, David S Lee, Mei-Cheng Wang, Susumu Mori, Richard O'Brien, et al., The diffeomorphometry of temporal lobe structures in preclinical Alzheimer's disease, NeuroImage: Clinical 3 (2013) 352–360.
[38] Shahrooz Faghih Roohi, Reza Aghaeizadeh Zoroofi, 4D statistical shape modeling of the left ventricle in cardiac mr images, Int. J. Comput. Assist. Radiol. Surg. 8 (2013) 335–351.
[39] Xavier Pennec, Radu Stefanescu, Vincent Arsigny, Pierre Fillard, Nicholas Ayache, Riemannian elasticity: A statistical regularization framework for non-linear registration, in: Medical Image Computing and Computer-Assisted Intervention–MICCAI 2005: 8th International Conference, Palm Springs, CA, USA, October 26-29, 2005, Proceedings, Part II 8, Springer, 2005, pp. 943–950.
[40] Stefan Sommer, Mads Nielsen, François Lauze, Xavier Pennec, A multi-scale kernel bundle for LDDMM: towards sparse deformation description across space and scales, in: Information Processing in Medical Imaging: 22nd International Conference, IPMI 2011, Kloster Irsee, Germany, July 3-8, 2011. Proceedings 22, Springer, 2011, pp. 624–635.
[41] Reza Zolfaghari, Nicolas Epain, Craig T Jin, Anthony Tew, Joan Glaunes, A multiscale lddmm template algorithm for studying ear shape variations, in: 2014 8th International Conference on Signal Processing and Communication Systems, ICSPCS, IEEE, 2014, pp. 1–6.
[42] Roy Kerckhoffs, Jeffrey Omens, Andrew McCulloch, A single strain-based growth law predicts concentric and eccentric cardiac growth during pressure and volume overload, Biophys. J. 102 (3) (2012) 353a.
[43] Suniti Yadav, Correlation analysis in biological studies, J. Pract. Cardiovasc. Sci. 4 (2) (2018) 116–121.
[44] Du Hanxiao, Sun Luming, Chen Songchang, Yang Jingmin, Zhang Yueping, Zhang Shuo, Chen Hongyan, Jiang Ning, Lu Daru, Noninvasive prenatal prediction of fetal haplotype with spearman rank correlation analysis model, Mol. Genet. Genom. Med. 10 (8) (2022) e1988.
[45] David N Reshef, Yakir A Reshef, Hilary K Finucane, Sharon R Grossman, Gilean McVean, Peter J Turnbaugh, Eric S Lander, Michael Mitzenmacher, Pardis C Sabeti, Detecting novel associations in large data sets, Science 334 (6062) (2011) 1518–1524.
[46] Debao Guan, Xin Zhuan, William Holmes, Xiaoyu Luo, Hao Gao, Modelling of fibre dispersion and its effects on cardiac mechanics from diastole to systole, J. Eng. Math. 128 (1) (2021) 1–24.
[47] Debao Guan, Faizan Ahmad, Peter Theobald, Shwe Soe, Xiaoyu Luo, Hao Gao, On the AIC-based model reduction for the general Holzapfel–Ogden myocardial constitutive law, Biomech. Model. Mechanobiol. 18 (4) (2019) 1213–1232.
[48] H. Gao, W.G. Li, L. Cai, C. Berry, X.Y. Luo, Parameter estimation in a holzapfel–ogden law for healthy myocardium, J. Eng. Math. 95 (2015) 231–248.
[49] Debao Guan, Hao Gao, Li Cai, Xiaoyu Luo, A new active contraction model for the myocardium using a modified hill model, Comput. Biol. Med. 145 (2022) 105417.
[50] Stanley Durrleman, Marcel Prastawa, Nicolas Charon, Julie R Korenberg, Sarang Joshi, Guido Gerig, Alain Trouvé, Morphometry of anatomical shape complexes with dense deformations and sparse parameters, NeuroImage 101 (2014) 35–49.
[51] Timothy A. Burkhart, David M. Andrews, Cynthia E. Dunning, Finite element modeling mesh quality, energy balance and validation methods: A review with recommendations associated with the modeling of bone tissue, J. Biomech. 46 (9) (2013) 1477–1488.